The Astrophysical Journal, 682:1338–1350, 2008 August 1

THREE-DIMENSIONAL MAGNETOHYDRODYNAMIC WAVE BEHAVIOR IN ACTIVE REGIONS: INDIVIDUAL LOOP DENSITY STRUCTURE

J. A. McLaughlin[1] and L. Ofman
Catholic University of America, NASA Goddard Space Flight Center, Code 671, Greenbelt, MD 20771; james@mcs.st-and.ac.uk
Received 2007 May 10; accepted 2008 March 21

ABSTRACT

We present the numerical results from a three-dimensional (3D) nonlinear MHD simulation of wave activity in an idealized active region in which individual, realistic loop density structure is included. The active region is modeled by an initially force-free, dipole magnetic configuration with gravitationally stratified density and contains a loop with a higher density than its surroundings. This study represents an extension to the model of Ofman & Thompson. As found in their work, we see that fast wave propagation is distorted by the Alfvén speed profile and that the wave propagation generates field line oscillations, which are rapidly damped. We find that the addition of a high-density loop significantly changes the behavior inside that loop, specifically in that the loop can support trapped waves. We also find that the impact of the fast wave impulsively excites both horizontal and vertical loop oscillations. From a parametric study of the oscillations, we find that the amplitude of the oscillations decreases with increasing density contrast, whereas the period and damping time increase. This is one of the key results presented here: that individual loop density structure can influence the damping rate, and specifically that the damping time increases with increasing density contrast. All these results were compared with an additional study performed on a straight coronal loop with similar parameters. Through comparison with the straight loop, we find that the damping mechanism in our curved loop is wave leakage due to curvature. The work performed here highlights the importance of including individual loop density structure in the modeling of active regions and illustrates the need for obtaining accurate density measurements for coronal seismology.

Subject headings: MHD — Sun: corona — Sun: magnetic fields — Sun: oscillations — waves

Online material: color figures, mpeg animations

1. INTRODUCTION

Coronal loop oscillations associated with impulsive events such as flares and coronal mass ejections (CMEs) have now been observed numerous times with the *TRACE* satellite (Nakariakov et al. 1999; Aschwanden et al. 1999, 2002; Wang & Solanki 2004) and recently by the *Hinode* satellite (Ofman & Wang 2008). One of the key results found in all these observations is that in most cases the loop oscillations decay rapidly within a few periods. Several proposed theories have been put forward to explain this strong damping, including enhanced viscosity (Nakariakov et al. 1999), wave leakage (Brady & Arber 2005; Terradas et al. 2005a), phase mixing with enhanced resistivity (Ofman & Aschwanden 2002), and resonant absorption (Ruderman & Roberts 2002). Comprehensive reviews of the different damping mechanisms can be found in Roberts (2004) and § 7.5 of Aschwanden (2004). Although a great deal of analytical work has been done on these damping mechanisms, their presence and the relative importance of each under realistic coronal conditions is not yet clear. It is most likely that a detailed and numerical treatment of a realistic coronal loop, together with high-resolution and spectral observations, is required to gain further understanding of the problem (Roberts 2000).

Active regions are magnetic structures in the solar corona and are associated with areas of concentrated magnetic field and increased temperature and density, and they are dynamic in nature. However, the dynamics, heating, and stability of active regions are not yet fully understood. The behavior of MHD waves and transient perturbations within active regions depends on many factors, such as the magnetic field strength, local magnetic topology, temperature, and density structure. Thus, the propagating characteristics of the waves provide information on the local fast magnetoacoustic speed, allowing one to infer the structure of the corona and ultimately determine the three-dimensional magnetic field. Recent observations of wave activity by the *SOHO*, *TRACE*, and *Hinode* satellites, coupled with measurements of photospheric magnetograms and three-dimensional numerical models, have improved our understanding of active regions. The detection of these coronal waves and three-dimensional modeling provides us with a new diagnostic tool for obtaining the parameters of the corona: coronal seismology.

Coronal seismology was first suggested by Uchida (1970) and later discussed by Roberts et al. (1984). Nakariakov & Ofman (2001) demonstrated that the coronal loop oscillations can be used to determine the magnetic field of an oscillating loop. Other studies include those of Wang et al. (2003a, 2003b), who investigated slow-mode standing waves with SUMER, and Williams et al. (2001, 2002), who reported on propagating fast waves with the Solar Eclipse Corona Imaging System (SECIS). Reviews of coronal seismology can be found in De Moortel (2005), Nakariakov & Verwichte (2005), and Banerjee et al. (2007). Low-amplitude Alfvén waves were detected recently throughout the corona with a ground-based coronagraph (Tomczyk et al. 2007). Recently, coronal seismology was developed extensively in several studies (Arregui et al. 2007; Ballai 2007; Erdélyi & Verth 2007; Gruszecki et al. 2007; Ofman 2007; Selwa et al. 2007; Taroyan et al. 2007; Van Doorsselaere et al. 2007; Verth et al. 2007; Wang et al. 2007; Ofman & Wang 2008).

Here we focus on the behavior of MHD waves in active regions, with potential applications to coronal seismology and the study of oscillation damping. The first studies of 3D MHD models of wave activity in coronal active regions were performed by Ofman & Thompson (2002), in which they modeled the propagation

[1] Present address: School of Mathematics and Statistics, University of St. Andrews, St. Andrews, Fife KY16 9SS, UK.

of a fast magnetoacoustic wave within a 3D dipole magnetic configuration. They found that the wave undergoes strong reflection and refraction and that the general behavior was in agreement with observations. Terradas & Ofman (2004) extended the model to incorporate a potential field extrapolation of a photospheric magnetogram. Again, they found that the main features of the simulation matched those of the waves observed with *TRACE*. More recently, Ofman (2005, 2007) demonstrated the potential of such models: that the analysis of such three-dimensional wave propagation can serve as a diagnostic of active region parameters.

The main limitation of these studies has been that the individual loop density structure was not included. The inclusion of such loops creates a density contrast between the loop and the ambient plasma, and this can support trapped MHD modes (Roberts et al. 1983), as well as phase mixing (Heyvaerts & Priest 1983) and resonant absorption (Ionson 1978; Davila 1987; Hollweg 1987; Goossens et al. 1992; Steinolfson & Davila 1993; Ofman et al. 1994, 1995; Ofman & Davila 1995; Goossens et al. 1995; Ruderman & Roberts 2002), in the loops. This paper aims to contribute to the understanding of wave activity in coronal active regions by including an individual high-density loop in an idealized active region. Note that there are considerable difficulties in the interpretation and modeling of the oscillations due to mode coupling in inhomogeneous MHD fluids and nonlinear effects. Thus, to clearly demonstrate the effects of adding individual loop density structure to the model, the work here is presented as an extension to that of Ofman & Thompson (2002), which from now on will be referred to as Paper I.

Finally, we note that Terradas et al. (2006b) studied kink modes of oscillation in a curved coronal loop using a linear, $\beta = 0$ toroidal model with a power-law density profile. By considering linearized perturbation about this equilibrium, Terradas et al. found two types of fundamental kink modes with either (mainly) horizontal or vertical polarizations. It was also noted that the oscillations were damped and that this was due to resonant absorption and wave leakage, with the former being the dominant damping mechanism. In the work presented below, we approach this problem with a much more realistic model by solving the nonlinear resistive 3D MHD equations with finite β, and our model contains nonlinear interactions, which are important in the initial stages of the oscillations, as well as coupling to compressional modes. In addition, Terradas et al. (2006b) considered a density contrast of $\xi = 3$, whereas in this paper we investigate the effect of the density contrast over a range of values.

The outline of the paper is as follows. In § 2, we present descriptions of the methodology and techniques used in the construction of the simulations, including the MHD equations solved and the initial and boundary conditions used. The inclusion of the density structure of individual, realistic coronal loops is described in § 3. The numerical results are presented in § 4 and the conclusions are given in § 5. Finally, a straight loop study and analytical work are included as appendices.

2. THREE-DIMENSIONAL MHD MODEL

We solve the normalized, three-dimensional, nonlinear, resistive MHD equations including gravitational effects:

$$\frac{\partial \rho}{\partial t} + \nabla \cdot (\rho \boldsymbol{v}) = 0, \tag{1}$$

$$\rho \left[\frac{\partial \boldsymbol{v}}{\partial t} + (\boldsymbol{v} \cdot \nabla) \boldsymbol{v} \right] = -\frac{\beta}{2} \nabla p + (\nabla \times \boldsymbol{B}) \times \boldsymbol{B} - \frac{\rho}{\mathrm{Fr}\,(R_\odot + z - z_{\min})^2} \hat{\boldsymbol{z}}, \tag{2}$$

$$\frac{\partial \boldsymbol{B}}{\partial t} = \nabla \times (\boldsymbol{v} \times \boldsymbol{B}) + \frac{1}{S} \nabla^2 \boldsymbol{B}, \tag{3}$$

$$\frac{\partial T}{\partial t} + (\boldsymbol{v} \cdot \nabla) T = -(\gamma - 1) T (\nabla \cdot \boldsymbol{v}) + (\gamma - 1)(H_{\rm in} - H_{\rm loss}), \tag{4}$$

where ρ is the mass density, $\boldsymbol{v}$ is the plasma velocity, $\boldsymbol{B}$ is the magnetic induction (usually called the magnetic field), p is the plasma pressure, $\hat{z}$ is a unit vector in the direction perpendicular to the photospheric plane in the locally cartesian coordinate system, $\mathrm{Fr} = V_0^2 L / G M_\odot$ is the Froude number (G is the gravitational constant, $M_\odot$ is the solar mass, $R_\odot$ is the solar radius, L is the typical length scale in the system, and V_0 is the typical speed in the system), $\beta = 2c_s^2/\gamma v_{\rm A}^2$ is the ratio of the thermal to the magnetic pressure [c_s is the sound speed, $v_{\rm A} = |\boldsymbol{B}|/(4\pi\rho)^{1/2}$ is the Alfvén speed, and γ is the ratio of specific heats], $S = LV_0/\eta$ is the Lundquist number (η is the resistivity), T is the temperature, $H_{\rm in}$ is the heat input due to coronal heating, and $H_{\rm loss}$ is the heat loss due to conduction, radiation, etc. Viscosity is neglected in the model presented here. Equations (1)–(4) were also presented, although in slightly different forms, in Ofman & Thompson (2002) and Ofman (2005, 2007).

For simplicity, we have assumed an isothermal plasma ($\gamma = 1$). Therefore, $p = \rho$ in normalized units and there is no need to solve the energy equation; i.e., the $\gamma = 1$ condition implies that the convective derivative of T is zero and thus the initially isothermal medium remains unchanged. The isothermal assumption is consistent with the observed global structure of active regions (Cirtain et al. 2006). Furthermore, we assume the same values of the parameters as in Paper I: i.e., $B_0 = 85$ G, $T_0 = 10^6$ K, $n_0 = \rho_0/m_p = 10^9$ cm^{-3} (where m_p is the proton mass), and $L = R_\odot/10 = 69{,}550$ km. Furthermore, $c_s = 128.5$ km s^{-1} (constant in our isothermal model), and the velocities and times were normalized by $V_0 = 5853$ km s^{-1} and $\tau_{\rm A} = 11.9$ s (Alfvén time).

The equations are solved with a modified Lax-Wendroff scheme with a fourth-order smoothing term. The divergence of the magnetic field is corrected with Powell's method. Details of the numerical code can be found in Paper I. The equations are solved in a computational box of dimensions $(x_{\min}, x_{\max}) \times (y_{\min}, y_{\max}) \times (z_{\min}, z_{\max})$, where $-x_{\min} = x_{\max} = -y_{\min} = y_{\max} = 3.5L, z_{\min} = L$, and $z_{\max} = 4.5L$. The resolution used in the simulations shown here was $150 \times 300 \times 150$.

2.1. *Boundary and Initial Conditions*

We take an idealized 3D potential dipole as the initial equilibrium magnetic field configuration for our active region (Fig. 1). The equations for this dipole can be found in Paper I. At the base of the corona ($z = z_{\min}$), we keep the magnetic field fixed, whereas we use zero-order extrapolation for the velocity and density:

$$\boldsymbol{B}(x, y, z_{\min}, t) = \boldsymbol{B}(x, y, z_{\min}, 0), \tag{5}$$

$$\boldsymbol{v}(x, y, z_{\min}, t) = \boldsymbol{v}(x, y, z_{\min} + \Delta z, t), \tag{6}$$

$$\rho(x, y, z_{\min}, t) = \rho(x, y, z_{\min} + \Delta z, t), \tag{7}$$

where Δz is the grid separation in the z-direction. We use open boundary conditions at the other five boundary planes. At $x_{\min}$ and $x_{\max}$, the boundary conditions are

$$\boldsymbol{B}(x_{\min,\max}, y, z, t) = \boldsymbol{B}(x_{\min,\max} \pm \Delta x, y, z, t), \tag{8}$$

$$\boldsymbol{v}(x_{\min,\max}, y, z, t) = \boldsymbol{v}(x_{\min,\max} \pm \Delta x, y, z, t), \tag{9}$$

$$\rho(x_{\min,\max}, y, z, t) = \rho(x_{\min,\max} \pm \Delta x, y, z, t), \tag{10}$$

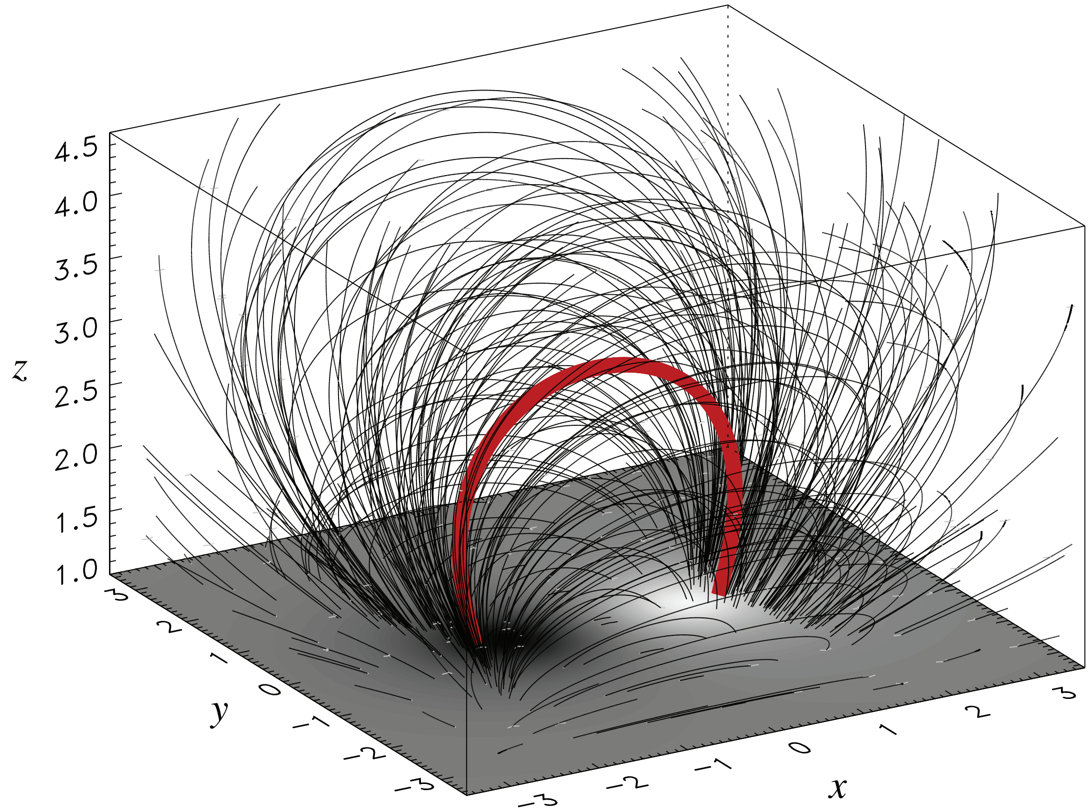

Fig. 1.—Three-dimensional structure of the initial potential magnetic field that we use to simulate our active region. The intensity plot at $z = 0$ of the B_z component shows the polarity of the field (dark indicates negative and bright indicates positive polarity). The field line that passes through the point $(x, y, z) = (0, 0, 3)$ is indicated in red. It is this field line that is used to construct our overdense loop. Note that here we have simply colored and thickened the field line in order to indicate the overdense loop (Fig. 3 shows the actual individual density stratification used in the model). [*This figure is available as an mpeg animation showing the impact of the wave in the electronic edition of the Journal.*]

where Δx is the grid separation in the x-direction. The plus sign corresponds to $x_{\rm min}$ and the minus sign to $x_{\rm max}$. We use similar expressions for the variables at $y_{\rm min, max}$ and $z_{\rm max}$.

The initial background density is given by solving the time-independent momentum balance equation (eq. [2] with $\boldsymbol{v} = 0$). When we recall that $p = \rho$ in our normalized units and that the Lorentz force is zero because of our choice of a potential magnetic configuration, this gives the gravitationally stratified hydrostatic density, which in our coordinate system is

$$\rho(x, y, z, 0) = \rho_0 \exp\left[\frac{1}{H}\left(\frac{1}{R_\odot + z - z_{\rm min}} - \frac{1}{R_\odot}\right)\right], \qquad (11)$$

where $H = 2/(\beta\,{\rm Fr}) = 2k_{\rm B}T_0R_\odot/10GM_\odot m_p$ is the normalized scale height ($k_{\rm B}$ is Boltzmann's constant). Using the normalization given above, $R_\odot = 10$ and $H = 8.7 \times 10^{-3}$, which corresponds to a scale height of 60.5 Mm. Thus, our z-range extends across approximately four scale heights.

The plasma β, which is the ratio of the magnetic pressure to the gas pressure, is very low in our system. At the center of the lower boundary, $\beta = 0.002$, while at the top, $\beta = 0.08$. Note that in our isothermal model, the sound speed is constant and so $\beta \sim v_{\rm A}^{-2}$. Thus, β varies throughout our computational box and has larger values in the outer parts of the domain (since the magnetic field strength is lower in these regions). Current estimates of the plasma β are around 0.07 and 0.2 for the cool and hot corona, respectively (Gary 2001).

To model the impact of a fast magnetoacoustic wave on the active region, we impose the following velocity pulse at the x-z boundary plane along $y = y_{\rm min}$:

$$V_y(x, y_{\rm min}, z, t) = Av_{\rm A}(x, y_{\rm min}, z) \quad \text{for } 0 \le t \le \delta t, \qquad (12)$$

where the duration of the pulse is $\delta t = 10\tau_{\rm A}$ and A is the initial amplitude of the pulse ($A = 0.25$ in the following simulations). After a short transit time ($5\tau_{\rm A}$) following the pulse, the boundary condition on V_y becomes open to allow flow through the boundary. This initial velocity leads to the formation of a fast magnetoacoustic wave in the computational domain. The phase speed of fast magnetoacoustic waves is given by

$$V_{\rm fast} = \left(\frac{1}{2}\left\{v_{\rm A}^2 + c_s^2 + \left[\left(v_{\rm A}^2 + c_s^2\right)^2 - 4v_{\rm A}^2c_s^2\cos^2\theta\right]^{1/2}\right\}\right)^{1/2}, \qquad (13)$$

where θ is the angle between the magnetic field and the propagating wave. In the low-β plasma of our model, $c_s \ll v_{\rm A}$, and so $V_{\rm fast} \approx v_{\rm A}$. Thus, understanding the Alfvén speed profile is crucial to understanding the propagation of the fast wave. The form of $V_{\rm fast}(x, y, z)$ in several planes can be seen in Figure 2. Note that equation (13) is derived for the modes of a homogeneous unbounded medium (e.g., Roberts 1981) and so is only an approximation in the context of this paper.

3. INDIVIDUAL LOOP DENSITY STRUCTURE

Dense loops with fine structure are commonly observed in the corona in the EUV (e.g., in *TRACE* observations), and these structures persist for long periods of time (days). Hence, the inclusion of individual loop density structure is a natural extension to the modeling of active regions (as discussed in Terradas & Ofman 2004, with first results by McLaughlin & Ofman 2006). As mentioned above, it is hoped that the inclusion of such 3D loops will shed light on the relative importance of the different damping

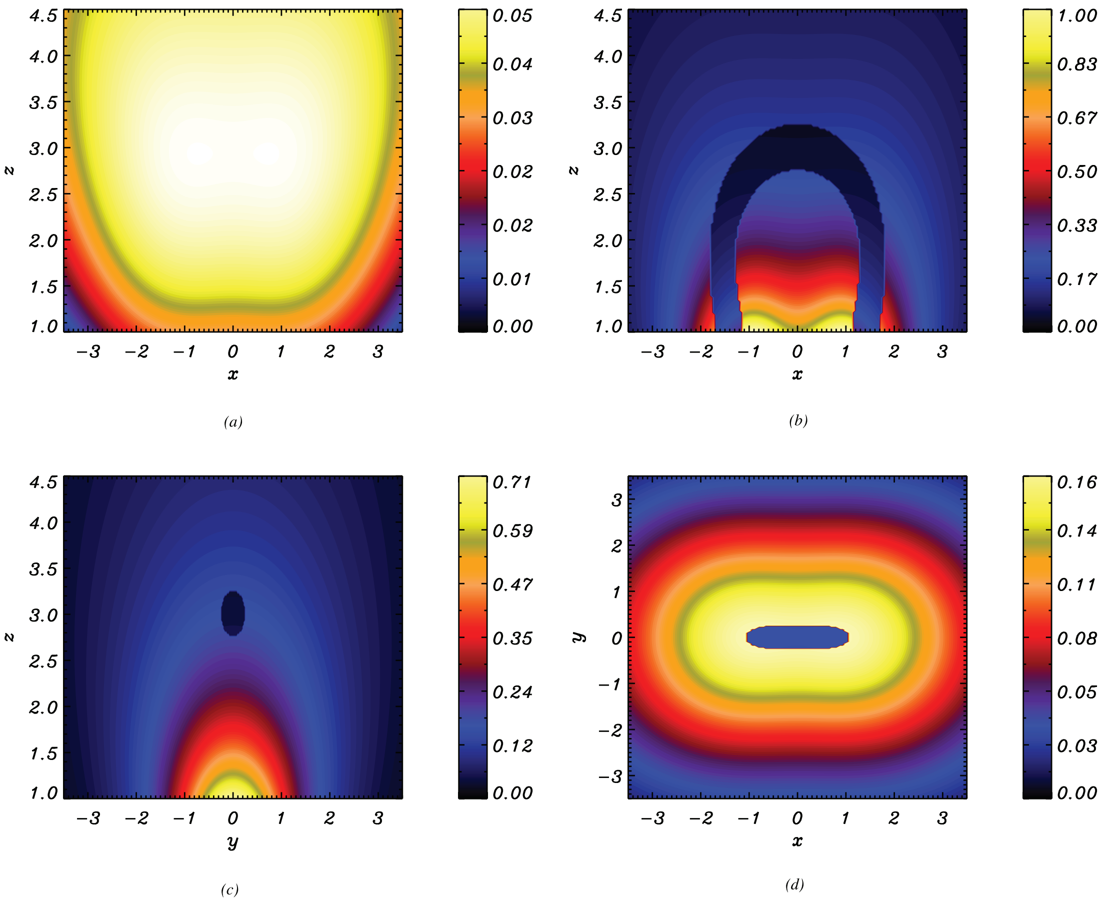

FIG. 2.—Fast magnetoacoustic speed in four planes of our computational box: (*a*) $V_{\rm fast}(x,\ -3.5,\ z)$ (the *x-z* plane along which we launch our velocity perturbation); (*b*) $V_{\rm fast}(x,\ 0,\ z)$ (the *x-z* plane through the center of the box, along $y = 0$), in which the loop can clearly be seen; (*c*) $V_{\rm fast}(0,\ y,\ z)$ (the *y-z* plane through the center of the box, along $x = 0$), in which the loop cross section can be seen; and (*d*) $V_{\rm fast}(x,\ y,\ 3)$ (the *x-y* plane through the apex of our high-density loop). The loop presented here has a density enhancement of $\xi = 10$. In our model, $c_s \ll v_{\rm A}$, and so $V_{\rm fast} \approx v_{\rm A}$.

mechanisms and will also allow quantitative comparisons to be made with observations of loop oscillations.

In past papers, models of curved coronal loops have used analytical density profiles in the setup of their systems (e.g., two-dimensional [2D] MHD models by Selwa et al. 2005b, 2006, 2007), which tend to be circular or elliptical loops (e.g., 2D MHD models by Brady & Arber 2005, and linear models by Díaz 2006; Díaz et al. 2006; Terradas et al. 2006b; Verwichte et al. 2006a, 2006b). Here we adopt a more general approach; we choose an individual field line from our magnetic configuration and use it as the axis for our loop. We then map the field line loop onto our 3D computational domain and increase the density in the loop in a given radius centered at the field line (thus modifying the Alfvén speed in that loop).

In this paper, we present a model with the inclusion of a single high-density loop in order to clearly demonstrate how the results change from those of Paper I. In this paper, we choose a field line that passes through the point $(x,\ y,\ z) = (0,\ 0,\ 3)$ (see Fig. 3). We use this field line as the axis of our loop and then choose its radius and density enhancement relative to the background (stratified) density as free parameters. Let us define this density enhancement as $\xi(s) = \rho_i(s)/\rho_0(s)$, where ρ_i is the density inside the loop, ρ_0 is the density outside, and s is the coordinate along the loop. For *TRACE* loops, the value of ξ is typically in the range 2–10 (Aschwanden 2004). Initially, we will consider $\xi = 10$, independent of s.

McLaughlin & Ofman (2006) first looked at including high-density loops in an active region model by increasing the density along individual field lines. However, they concluded that the results were affected by resolution and that the loop required a finite thickness and adequate resolution across the loop (their loops were in effect only one grid point thick). The model presented here addresses this issue by including a loop of finite thickness.

However, we cannot simply choose any density profile for our high-density loop. In order to have an equilibrium state at $t = 0$ of the MHD equations for our high-density loop, we must satisfy the time-independent momentum balance equation along the loop,

$$\frac{\beta}{2}\nabla p(s) + \frac{\rho(s)}{\rm Fr}\frac{1}{\left[R_\odot + z(s) - z_{\rm min}\right]^2}\hat{z} - [\nabla\times\boldsymbol{B}(s)]\times\boldsymbol{B}(s) = 0, \tag{14}$$

where s is the coordinate along the field line.

Since the plasma β is small in our system and the Lorentz force is zero, we are nearly free to choose the density distribution across the field lines but must still satisfy equation (14) *along* each field line. By solving equation (14) along each field line in our potential system ($\nabla\times\boldsymbol{B} = 0$), we obtain

$$\rho(s,\ \rho_i) = \rho_i \exp\left\{\frac{1}{H}\left[\frac{1}{R_\odot + z(s) - z_{\rm min}} - \frac{1}{R_\odot}\right]\right\}, \tag{15}$$

where ρ_i is the density at the point $s = 0$, which can be set at $z = z_{\rm min}$ (footpoint of the loop). Since equation (15) has the

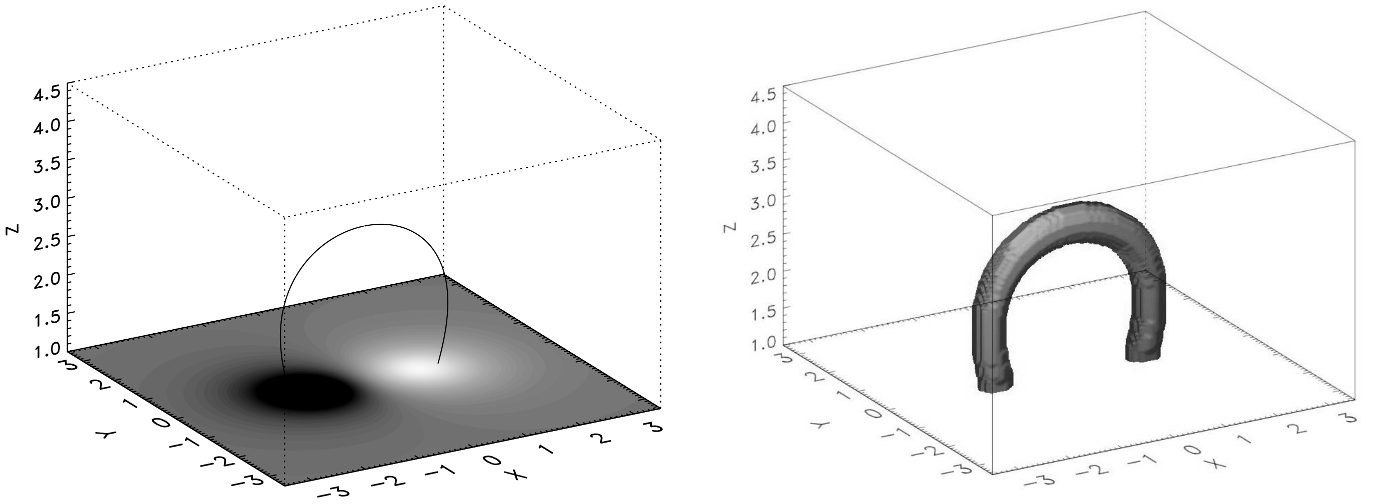

FIG. 3.—*Left*: Field line selected from our equilibrium magnetic field configuration that passes through the point $(x, y, z) = (0, 0, 3)$. *Right*: Loop constructed along this field line, with a length of 7.0, a chosen minor radius of 0.25, and a density enhancement of ξ relative to the background (stratified) density. [*See the electronic edition of the Journal for a color version of the right panel of this figure*.]

same form as equation (11), we find that the densities inside and outside the loop have the same scale height. Thus, ξ is independent of s for our model. Hence, it makes sense to talk of a density enhancement or density contrast for our loop and still retain that the system is gravitationally stratified.

Note that in the loop presented here, we chose a discontinuous jump between ρ_i and ρ_0 (for simplicity). In addition, the magnetic pressure holds the loop in place across the field lines with very small adjustments; i.e., the system settles into equilibrium before the wave is launched. The adjustments in the initial loop radius are small because the plasma β is $\ll 1$, and in fact we neglect the thermal pressure gradients due to the loop density variation across the field lines (effectively setting $\beta_\perp = 0$ in the initial state) so that we ignore the small-amplitude slow waves and surface waves that may be produced by the loop density structure, since we are predominantly interested in the (global) behavior of the fast wave. Finally, we note that the current could be nonzero in an observed non–force free loop structure. In that case, our high-density loop would have a more complicated form than that of equation (15), and one would need to solve equation (14) with the $(\nabla \times \boldsymbol{B}) \times \boldsymbol{B}$ term.

In the simulations presented below, we construct a loop of radius 0.25 at the footpoints, with a total length of 7.0 (i.e., radius $\ll$ length). In the active region, the radius of the loop slightly increases with height due to field divergence (remaining circular). We have chosen a computational domain of $(x, y) \in [-3.5, 3.5]$ and $z \in [1, 4.5]$, and consequently, our circular loop cross section appears elliptical in the y-z plane figures (solely due to our choice of axes). Aschwanden (2003) reports the average observed loop length as 220 ± 53 Mm (over a range of 74–582 Mm) and the average loop half-width as 4.4 ± 1.4 Mm (over a range of 2.8–8.4 Mm). We have chosen a loop length-to-radius ratio of 28 : 1, which is toward the lower limit of these observed values, but we have made this choice so that the radius will be fully resolved.

We have 300 grid points in the y-direction ($-3.5 \leq y \leq 3.5$) and 150 grid points in the z-direction ($1 \leq z \leq 4.5$). Hence, we have approximately 20 grid points across the loop in the y- and z-directions. We have less resolution across the structure in the x-direction (150 grid points over the range $[-3.5, 3.5]$), but this is where we expect the least activity (due to symmetry).

4. NUMERICAL RESULTS

In this section, we present results of the 3D MHD model computations of an active region subject to the initial and boundary conditions described above. The results presented in this paper are concerned with loop oscillations and wave damping, and how these effects vary with density contrast, ξ. Away from the loop, the behavior of the magnetic field, velocity, density and current is similar to that in Paper I. Thus, a full description of the behavior of these quantities is not given here, as all the results have previously been reported in that paper. We do, however, review some of the key results concerning the wave propagation, as this will greatly aid understanding of later sections.

4.1. *Velocity Behavior*

In Figure 4, we show the velocity evolution in the x-y plane along $z = 2.75$, i.e., a horizontal cut halfway through our box (*top*), and in the y-z plane along $x = 0$ (*bottom*), at three time slices. The arrows show the direction of the flows, and the red color scale indicates the magnitude of the variable in this plane. The blue shading indicates the location of the higher density loop (here $\xi = 10$). There are three key points to note:

1. Consider the x-y plane (Fig. 4, *top*). The wave front is clearly distorted by the nonuniform Alfvén speed in the active region. Initially, the central part propagates faster than the outlying regions due to the stronger magnetic field. The wave is reflected at the regions of high Alfvén speed, and this occurs close to $y = 0$ (recall Fig. 2*d*). The resultant wave consists of a reflected part (toward the negative y-direction) and a small transmitted component. Thus, the velocities in the $y = 0$ plane are very small, and hence the oscillations that occur there are small (weak impulsive excitation).

2. Consider the y-z plane (Fig. 4, *bottom*). Again, the wave front is distorted by the nonuniform Alfvén speed. From the arrows, we can see that the wave is deflected by the curved field toward the footpoints of the magnetic loops. Since the boundary conditions require that the magnetic field be fixed at the lower boundary, the waves are reflected near the footpoints. These reflected waves are present in the left-hand side of the active region, since the footpoint reflection is directed toward the negative y-direction. Thus, the high Alfvén speed in the center of the dipole (see Fig. 2*c*) acts as a barrier to the wave propagation.

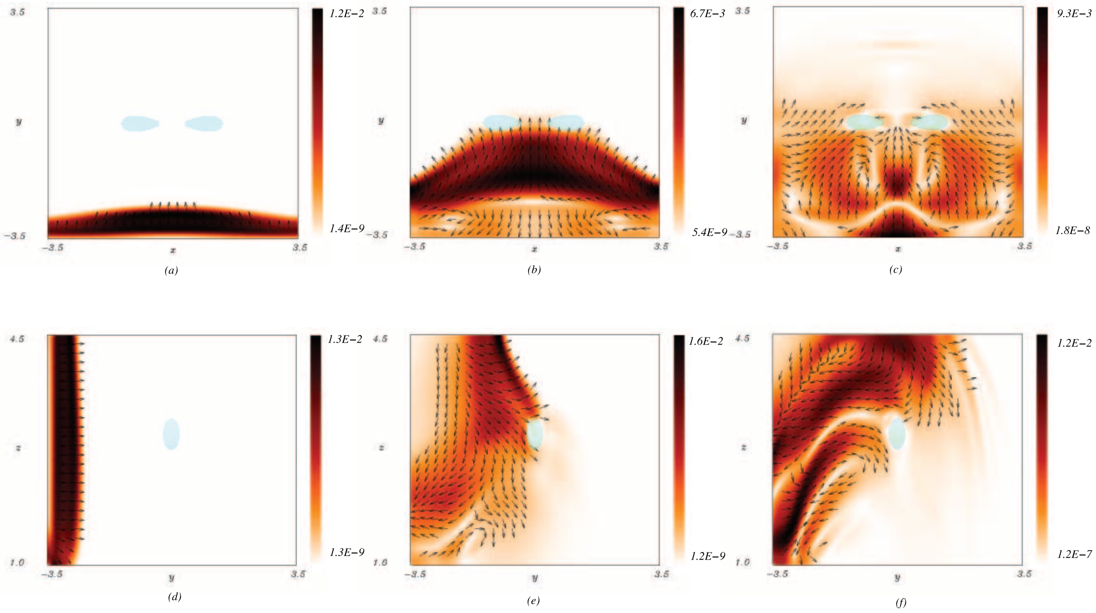

Fig. 4.—*Top row*: Velocity in the *x-y* plane at $z = 2.75$ of the incoming wave at the (Alfvén) times (*a*) $t = 12.8$, (*b*) $t = 33.5$, and (*c*) $t = 51.0$. The arrows show the direction of the flows, and the (red) color scale indicates the magnitude of the variable. *Bottom row*: Velocity in the *y-z* plane at $x = 0$ of the incoming wave at the same (Alfvén) times: (*d*) $t = 12.8$, (*e*) $t = 33.5$, and (*f*) $t = 51.0$. The blue shading indicates the location of the higher density curved loop (here $\xi = 10$). The wave propagates from the *x-y* plane into the 3D dipole. It is evident that the wave front is distorted by the nonuniform fast magnetoacoustic speed. [*Both the top and bottom rows of this figure are available as mpeg animations in the electronic edition of the Journal.*]

3. An important point to note for this paper is that when the fast wave first reaches the loop [the blue shaded region with apex located around $(x, y, z) = (0, 0, 3)$], there is flow in both the *y*-direction (V_y) and the *z*-direction (V_z). This behavior will be seen later in the temporal evolution subsection.

Thus, one of the key results is that the fast wave that was initially propagating in the positive *y*-direction has been partially reflected backward, to the sides and over the active region. It is important to note that the Alfvén speed profile dominates the propagation of the fast wave in the active region; specifically, the wave is refracted away from regions of high Alfvén speed. This refraction of fast wave propagation has been reported in several systems (e.g., Nakariakov & Roberts 1995; McLaughlin & Hood 2004, 2006) and was present in Paper I. In addition, it may explain why only a small number of loops are seen to oscillate in *TRACE* observations (this is discussed in § 5).

4.2. *Temporal Evolution*

In Figure 5, we show the temporal evolution of the velocity components, perturbed magnetic field components, and perturbed density at a point $(x, y, z) = (0, 0, 3)$, which is located inside and near the apex of our high-density loop. The oscillations seen at this point represent the response of these variables resulting from the impact of the fast magnetoacoustic wave. We present a comparison of two systems: the red lines represent the temporal evolution of quantities from a system with a high-density loop with $\xi = 10$, and the blue lines come from a system with $\xi = 1$; i.e., the system studied in Paper I (no density contrast). Thus, this figure demonstrates how the quantities have changed due to the addition of high density to the magnetic loop.

Let us first consider Figure 5*b*. In the $\xi = 1$ system (*blue line*), the first peak in V_y at $t = 384$ is due to the impact of the fast wave (there are corresponding variations in ΔB_y and Δn). After this time, the field line has been displaced and oscillates back and forth about its original position (approximately once). Thus, the second peak in V_y is due to the field line returning to its original position. However, in the $\xi = 10$ case (*red line*), we have different behavior. The first peak in V_y occurs at a slightly later time ($t = 392$), and then several oscillations occur. These oscillations are similar to those seen in the straight loop case (see Appendix A). There is also increased activity in Δn. In addition, we see that the magnetic pulse associated with the impact of the fast wave passes through $(x, y, z) = (0, 0, 3)$ at a later time (see Fig. 5*c*). This is expected since the Alfvén speed in the loop is now reduced, and so the fast wave travels at a reduced speed.

Here it is instructive to mention the work of Terradas et al. (2005b, 2006a), in which the authors investigated the excitation and damping of trapped and leaky modes in one-dimensional (1D) and 2D coronal slabs and loops. It was found that the loop oscillated as a result of an initial disturbance and that, after a short transient phase, the loop displayed trapped normal modes. This transient phase, which is the initial response to the incoming perturbation followed by the excitation of leaky modes, was called the *impulsive leaky phase*, after which the dynamics are dominated by the (undamped) trapped mode, which is called the *stationary phase* (Appendix A demonstrates the different phases in a straight cylinder). Thus, using this terminology, we see that in Figure 5*b*, the impulsive leaky phase occurs between (approximately) $t = 370$ and $t = 440$; i.e., representing the initial response of the loop (also see Fig. 6). This is followed by a series of damped oscillations, which in our curved loop occurs in place of the stationary phase. However, one has to be cautious when comparing linear $\beta = 0$ theory (i.e., Terradas et al. 2006b) with nonlinear 3D MHD results. For example, in our model the initial damping can occur because of nonlinear coupling between modes, as well as coupling to the slow mode (similar to Selwa et al. 2007), whereas these effects are not present in linear, $\beta = 0$ theory.

In addition, we see significant changes in the behavior of V_z in Figure 5*a*. In the $\xi = 1$ system, the evolution of V_z is related to the large-scale velocity flow in the active region: namely, a peak at $t = 367$ due to the fast wave being refracted upward away from the active region, and then $V_z < 0$ behavior related to the fast wave being deflected by the curved field toward the footpoints of

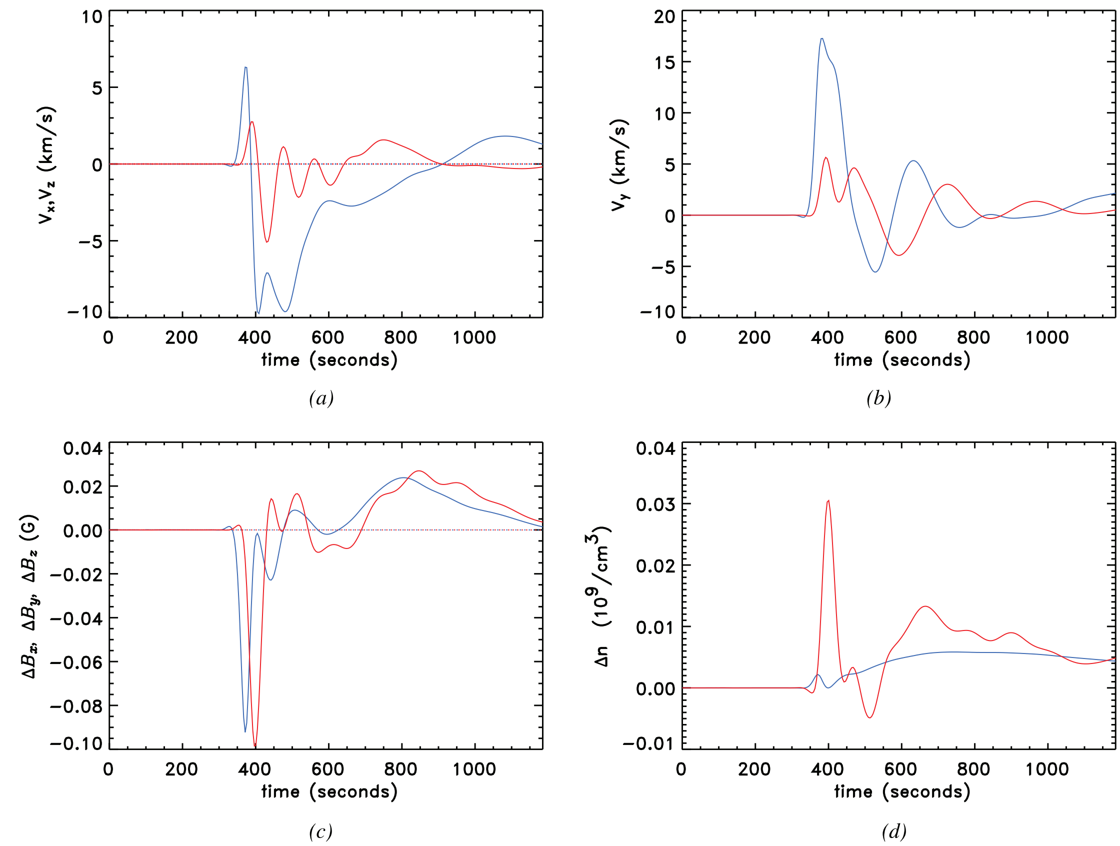

FIG. 5.—Comparison of the time evolution of several quantities at the point (0, 0, 3) between two systems with $\xi = 1$ (*blue lines*) and $\xi = 10$ (*red lines*) in our curved loop. The system with $\xi = 1$ is equivalent to the system described in Paper I. (*a*) V_x (*dotted lines*; ≈ 0) and V_z (*solid lines*). (*b*) V_y. (*c*) ΔB_x (*solid lines*), ΔB_y (*dotted lines*; ≈ 0), and ΔB_z (*dashed lines*; ≈ 0). (*d*) Δn.

the magnetic loops (as seen in Fig. 4*e*). However, in the $\xi = 10$ system, $V_z(0, 0, 3)$ exhibits very different evolution: a decaying oscillation that is related to the internal structure and trapped oscillations inside the high-density loop. Again, this evolution is comparable to that seen in the straight cylindrical loop case (Appendix A). However, it is possible to see the link between the two systems: in the $\xi = 1$ loop, there is an initial $V_z > 0$ disturbance (at $t = 367$) and then subsequent $V_z < 0$ flow, whereas in the $\xi = 10$ loop, there is again the same initial $V_z > 0$ disturbance (at $t = 388$; later because of the lower Alfvén speed), and this acts as the impulsive excitation that leads to the observed oscillations in V_z.

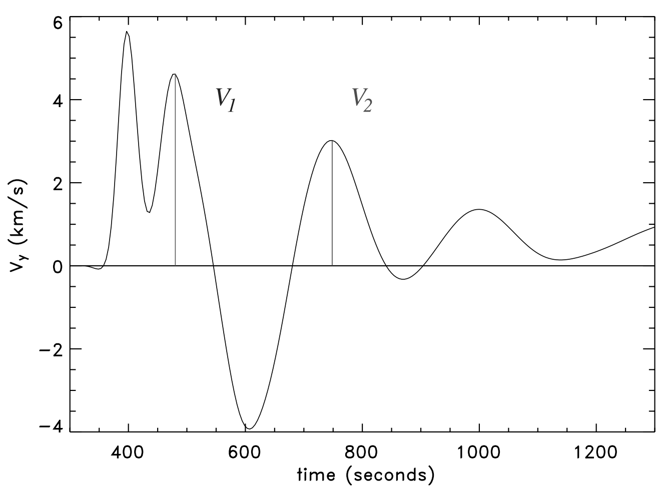

FIG. 6.—Time evolution of $V_y(0, 0, 3)$ in our curved loop with a density enhancement of $\xi = 10$. The impulsive leaky phase occurs between (approximately) $t = 370$ and $t = 440$, and this is followed by a series of damped oscillations. The amplitudes V_1 and V_2 are used to calculate the damping time, τ. Note that the final trend is not the initial unperturbed state.

In both systems, the loop experiences impulses of comparable magnitude in both V_y and V_z, and these impulses generate oscillations in the field. Due to the symmetry along $x = 0$ (note that the equilibrium magnetic field and the initial perturbation are symmetric in the y-z plane along $x = 0$), there is negligible magnitude of V_x in both systems. Thus, the point (0, 0, 3) is a node of V_x, and so we would expect the slow mode to be zero at this point. Theoretical works on the behavior of the slow mode in coronal loops can be found in Nakariakov et al. (2000) and Selwa et al. (2005a, 2007), as well as references therein. Finally, the amplitude of the oscillations is clearly reduced in the $\xi = 10$ system. A full parametric study of this variation in amplitude is discussed in § 4.4.

4.3. *Density Evolution*

As can be seen in Figure 1, the field lines respond to the propagation of the fast wave and oscillations are induced. The magnetic field response to the impact of the wave can be seen as an animation in the electronic edition of the *Journal*. These oscillations occur in the field lines and are sustained by the elastic nature of the magnetic field (magnetic tension is the restoring force). Correspondingly, the impact of the fast wave has caused oscillations in our loop, since the magnetic field is nearly frozen into the plasma (the Lundquist number is much greater than unity).

Thus, we should be able to see these oscillations in density, and this can be seen in Figure 7 (with $\xi = 10$). Since the perturbations are very small (as noted in § 4.1), the results are best seen as

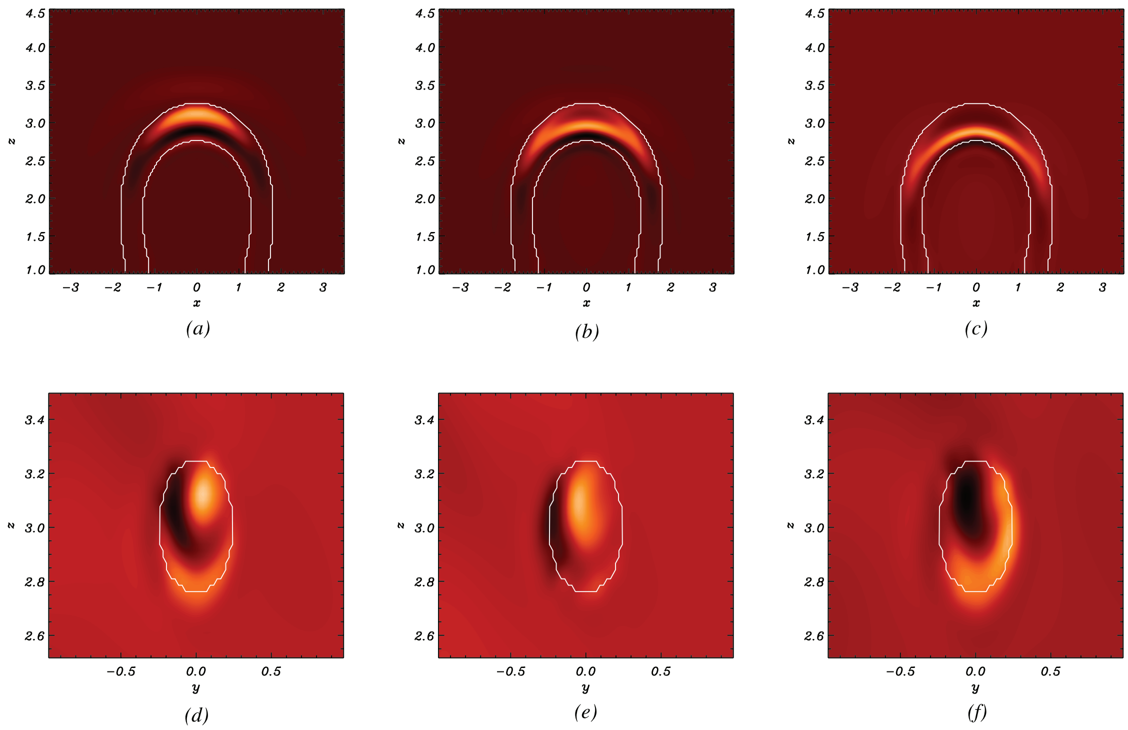

FIG. 7.—*Top row*: Difference images of the density in the *x-z* plane ($y = 0$) at the (Alfvén) times (*a*) $t = 31.5$, (*b*) $t = 33.5$, and (*c*) $t = 35.5$. Darker areas correspond to decreases in density, and lighter areas correspond to increases in density. *Bottom row*: Difference images of the density in the *y-z* plane ($x = 0$) at the same (Alfvén) times: (*d*) $t = 31.5$, (*e*) $t = 33.5$, and (*f*) $t = 35.5$. Note that in order to see the results more clearly, we have changed the range in the *y-z* plane to focus on the area around the high-density curved loop. In all panels, the white outline indicates the initial location of the high-density loop.

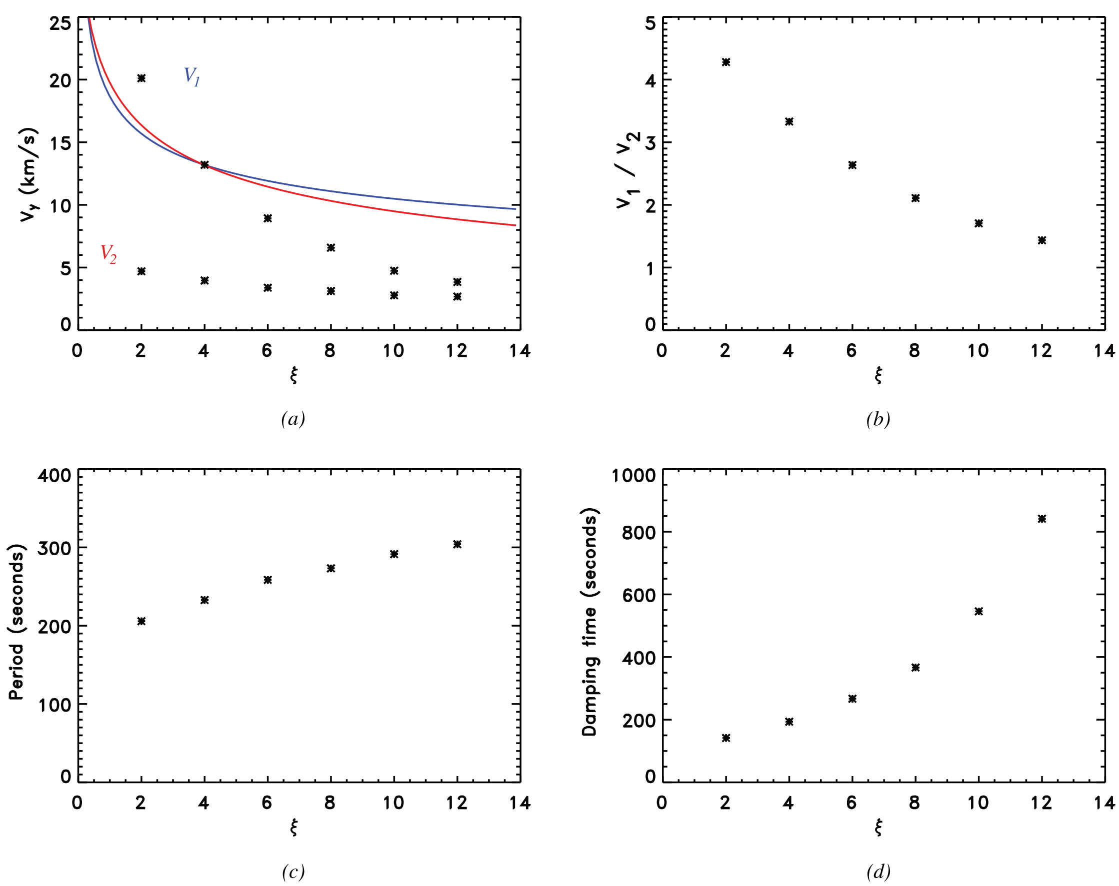

FIG. 8.—Curved loop. (*a*) V_1 (*upper set of asterisks*) and V_2 (*lower set of asterisks*; from V_y) as a function of ξ. The blue line represents the WKB wave propagation analytical solution. The red line represents the reflection/transmission coefficient solution. Both solutions have been normalized to $V_y(0, 0, 3)$ at $\xi = 4$ for clear comparison. (*b*) Ratio of V_1 to V_2 as a function of ξ. (*c*) Period of the oscillation (in units of seconds) as a function of ξ. (*d*) Damping time of the oscillation (in units of seconds) as a function of ξ.

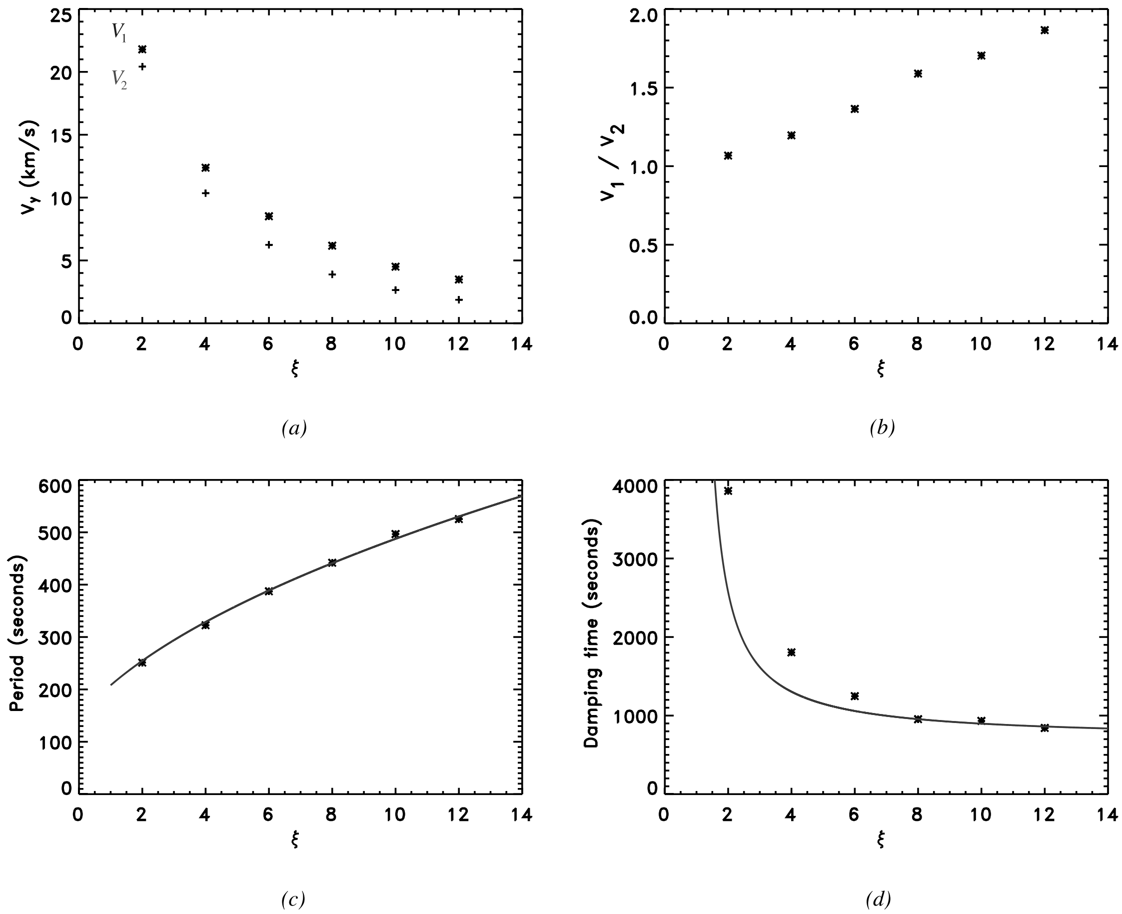

FIG. 9.—Straight loop. (*a*) V_1 (*asterisks*) and V_2 (*plus signs*), from V_y, as functions of ξ. (*b*) Ratio of V_1 to V_2 as a function of ξ. (*c*) Period of the oscillation (in units of seconds) as a function of ξ. The solid line represents the analytical solution of Edwin & Roberts (1983). (*d*) Damping time of the oscillation (in units of seconds) as a function of ξ. The solid line represents the analytical solution of Hollweg & Yang (1988). [*See the electronic edition of the Journal for a color version of this figure.*]

moving difference images (i.e., the previous image is subtracted from the current image), where the darker areas correspond to a decrease in density and lighter areas correspond to an increase in density. In the top row of Figure 7, we see the variation in the density in the *x-z* plane, and it is clear that the density equilibrium has been perturbed such that an oscillatory pattern appears. There are two possible reasons for this variation: either the loop is expanding and contracting in the vertical plane, or else we are seeing the projection effect of oscillations in the horizontal plane. These two types of modes can be classified as vertical or horizontal polarizations (according to the dominant component of the velocity field) and have been looked at theoretically by Díaz et al. (2006) and Terradas et al. (2006b). In particular, Terradas et al. found that these two types of polarization have a very similar frequency. It is important to distinguish between the two types as, for example, an oscillation in the vertical plane requires a change in the length of the loop and thus has consequences in coronal seismology.

We can distinguish whether we are seeing oscillations in the vertical or horizontal plane by looking at the density in the *x-z* plane. This can be seen in the bottom row of Figure 7. Note that in order to see the results more clearly, we have changed the range of the axes to focus on the area around the high-density loop. We see that we have a superposition of *both* horizontal (dark next to light) and vertical oscillations (dark above light, or vice versa). Horizontal and vertical polarizations were recently seen in observations by Wang & Solanki (2004) and were looked at theoretically by Selwa et al. (2005b).

These oscillations are in agreement with the interpretation of Figures 5*a* and 5*b*: i.e., that the apex of the loop is impacted by the fast wave in both V_y and V_z. For example, in Figure 7*c* it appears that the loop is oscillating in the vertical plane, but by comparing with Figure 7*e*, we see that it is in fact oscillating in both planes. Correspondingly, at this time the velocity at this point is $V_y > 0$ and $V_z < 0$. Thus, whether the loop experiences a vertical or horizontal oscillation is entirely determined by the velocity vector at that point.

4.4. *Parametric Study of ξ*

In § 4.2, it was noted that the amplitude and nature of the loop oscillations changed when the density ratio was increased from $\xi = 1$ to $\xi = 10$. This section examines the nature of that dependence further. Here we focus our investigation on the wave behavior seen in V_y, as this component clearly shows the field line oscillations. Figure 6 shows an enlarged version of Figure 5*b* for the $\xi = 10$ system. As mentioned above, and using the terminology of Terradas et al. (2005b, 2006a), we see that the impulsive leaky phase occurs between (approximately) $t = 370$ and $t = 440$, after which the loop displays damped oscillations: i.e., a secondary phase. Ignoring the impulsive leaky phase and considering the remaining part of the series, we use the amplitudes V_1 and V_2, which occur at times t_1 and t_2, to calculate the period of oscillation and the damping time, for several values of ξ. These quantities can be seen in Figure 8. We also compare and contrast our results with those for a straight cylinder with similar parameters (see Appendix A, and compare with Fig. 9).

Figure 8*a* shows how the amplitudes of V_1 and V_2 vary for different values of ξ. We can see that the amplitudes of both V_1 and V_2 decrease with increasing ξ. In addition, the behavior of V_1 is in good agreement with that of the straight cylinder model (Fig. 9*a*). However, the behavior of V_2 shows a different dependency on ξ from that of the straight cylinder model. We tried to fit the data using two analytical functions:

1. a function proportional to $\xi^{-1/4}$, which is the analytical dependence predicted by a WKB wave propagation model, and
2. a function proportional to the reflection/transmission coefficient at the loop boundary; i.e., proportional to $(1+\sqrt{\xi})^{-1}$.

However, neither analytical solution fits the simulation data perfectly, as can be seen in Figure 8*a*. The derivation of these analytical expressions can be found in Appendix B.

In Figure 8*b*, we see that the ratio of V_1 to V_2 also changes with ξ, confirming that V_1 and V_2 have different dependencies on ξ (and that these dependencies are more complicated than simple power laws). However, the magnitude and trend is different from that of a straight cylinder. This is due to the different behavior of V_2 in both models: i.e., the magnitude of V_2 is substantially lower in the curved model than in the straight cylinder, and so this affects the ratio of V_1 to V_2 and thus will affect the damping time (see below).

Figure 8*c* shows the period of oscillation at the point (0, 0, 3) as a function of ξ. The period, *P*, is calculated from $P = t_2 - t_1$. The period of oscillation increases with ξ. This is in agreement with the straight loop model. However, the period of oscillation in the straight loop case is longer (1–3 times; Fig. 9*c*).

We can fit the damped oscillations of V_y using the function

$$V_y(t) = A_0 \sin(t/P + \phi)e^{-t/\tau}, \tag{16}$$

where A_0 is a constant, τ is the damping time, i.e., the time taken for the oscillation to decrease in amplitude by *e* (the base of the natural logarithm), and ϕ is the phase difference. Thus, by using the amplitudes and times at two points of an oscillation, i.e., V_1 and V_2 at t_1 and t_2, we can obtain τ. Using this methodology, we can calculate $\tau = P/\ln(V_1/V_2)$. Figure 8*d* shows the damping time of the excited oscillations as a function of ξ. This graph provides one of the key results of this paper: we can see that damping time increases with increasing ξ.

By comparing this result with Figure 9*d*, we can see that the damping time is much shorter than that for the straight cylinder. Hence, the damping *rate* is greater in the curved loop. In addition, the dependence on ξ is reversed when comparing Figures 8*d* and 9*d*. This opposite behavior is addressed in § 5.

5. DISCUSSION AND CONCLUSIONS

We have presented for the first time the results from a 3D nonlinear MHD simulation of wave activity in active regions in which individual loop density structure is included. We have studied the behavior of a fast magnetoacoustic wave propagating within an active region composed from a 3D dipole, gravitationally stratified density and containing a loop with a higher density than its surroundings. We found that the fast wave propagation is distorted by the Alfvén speed profile and that the wave propagation generates (rapidly damped) loop oscillations.

We initially compared a system with a high-density loop of density contrast $\xi = 10$ and a system with $\xi = 1$ (equivalent to the system studied by Ofman & Thompson 2002). We found that the addition of a high-density loop significantly changes the behavior in that region; namely, that there was now internal oscillatory motion inside the loop. This was not surprising, as we would expect wave trapping to occur in a loop that is denser than its surroundings (Roberts et al. 1983). In addition, we found that the impact of the fast wave in both the V_y and V_z components impulsively excited both horizontal and vertical loop oscillations (Fig. 7). Subsequently, these oscillations were rapidly damped.

We found that the direction of the oscillation (i.e., whether vertical or horizontal) is determined by the velocity vector at that point in time, since the velocity behavior drives the oscillations. Thus, since the fast wave is distorted by the Alfvén speed in the 3D dipole, the wave impacts the loop in different places at different times. Hence, it is unlikely that the oscillation generated along the whole loop is the pure global kink mode.

We have restricted our work to studying an initial perturbation that impacts the equilibrium magnetic field symmetrically; i.e., it is symmetric in the *y*-*z* plane along $x = 0$. If our initial pulse were directed to form an angle with the dipole plane, we would expect the resultant oscillations to again exhibit both vertical and horizontal polarizations, but to also display *swaying* oscillations (Díaz et al. 2006).

We then performed a parametric study of the loop oscillations over a range of ξ-values. We focused our attention on the oscillations in V_y at the point $(x, y, z) = (0, 0, 3)$, as this clearly demonstrated the damped field line oscillations. We found that the amplitude of the oscillations decreases as ξ is increased, and that V_1 and V_2 display different dependencies on ξ. In addition, the period and damping time increase with increasing ξ, where the damping time was calculated using equation (16). This is one of the key results of this paper: that the individual loop density structure can influence the damping rate, and specifically that the damping time increases with increasing density contrast. This is not surprising, since the restoring force comes from magnetic tension, and so for a given magnetic field, denser loops are restored to equilibrium at a decreased rate due to increased inertia. These conclusions are consistent with those drawn by Smith et al. (1997), who found that for a 2D arcade the energy leakage is lower for slabs with a higher density ratio. However, our trend is not in agreement with Brady & Arber (2005), who found that for fast waves driven at the footpoints of a curved 2D flux tube, the decay time of the standing modes scales with the square root of ξ.

In addition, all these results were compared to a similar study performed on a straight coronal loop (Appendix A). It was found that the fast wave impulsively excites oscillations in the overdense cylinder, but that not all the oscillation is fully trapped. Looking at $V_y(0, 0, 3.5)$ inside our cylinder, we observe the initial passage of the pulse, followed by a transient phase (impulsive leaky phase), followed by the establishment of a trapped mode (stationary phase). The oscillation in the transient phase consists of nontrapped modes and normal modes, and the damping mechanism is wave leakage (i.e., leakage of the modes that are not normal modes). This leakage rate is determined by the density contrast. From Figure 9*d*, we see that the damping time decreases with increasing density contrast. This is in some agreement with the resonant absorption models of Ionson (1978), Hollweg & Yang (1988), and Ruderman & Roberts (2002; see eq. [17] below), although, as mentioned, the damping mechanism here is not due to resonant absorption, as we do not have thin layers at the cylinder boundary.

The damping time due to resonant absorption (e.g., Hollweg & Yang 1988; Goossens et al. 2002; Ruderman & Roberts 2002;

Aschwanden et al. 2003 and references therein) was derived by Ionson (1978) and Hollweg & Yang (1988) as

$$\tau_{\rm decay} \propto \frac{\rho_i + \rho_e}{\rho_i - \rho_e} P \quad \Rightarrow \quad \tau_{\rm decay} \propto \frac{(\xi + 1)^{3/2}}{\xi - 1}, \qquad (17)$$

where $\tau_{\rm decay}$ is the damping time, ρ_i is the internal density, ρ_e is the external density, P is the period, and $\xi = \rho_i/\rho_e$. This behavior can be seen as an overplot in Figure 9*d*. This damping time has been tested numerically by Steinolfson & Davila (1993). In addition, Poedts & Kerner (1991) and Arregui et al. (2005) found that the damping rate is independent of the magnetic diffusivity (although this is only true for resonant absorption).

Comparing the two systems (i.e., Figs. 8*d* and 9*d*), we find that the damping time is much longer in the straight loop system than in the curved. Thus, there must be additional effects that increase the damping rate in our curved loop. The increased damping rate is from the extra effect of wave leakage due to curvature in our system; i.e., we have used the straight loop study, which was set up with similar parameters, to rule out other possible damping mechanisms of viscosity and phase mixing. Wave leakage due to curvature has been studied extensively in the context of coronal loop oscillations (Smith et al. 1997; Van Doorsselaere et al. 2004; Murawski et al. 2005; Selwa et al. 2005b, 2006; Brady et al. 2006; Díaz et al. 2006; Díaz 2006; Verwichte et al. 2006a, 2006b; Terradas et al. 2006b).

It is also interesting to note that under damping due to curvature, the damping time increases as ξ increases, whereas in the straight cylinder model, the damping time *decreases* with ξ (from damping due to leakage of nontrapped modes). Thus, the two damping mechanisms exhibit opposite dependencies on ξ. However, the damping rate from wave leakage due to curvature is significantly greater (for the models and parameters we have presented here). In addition, from equation (17) we see that the damping time due to resonant absorption also decreases with ξ. Thus, it is interesting to note that damping due to resonant absorption exhibits the opposite dependency on ξ compared to wave leakage due to curvature.

We have also performed further investigations with a longer overdense loop: i.e., higher above the high Alfvén speed region. In this study, we choose a field line that passes through the point $(x, y, z) = (0, 0, 4)$. As before, we found that the field lines respond to the propagation of the fast wave and oscillations are induced (both horizontal and vertical polarizations). This study was conducted because it was thought that using a longer loop would produce a larger amplitude loop displacement compared to the loop studied above. However, even though the amplitudes of the oscillations are somewhat larger than those considered in the shorter loop studies, the behavior is very similar to that of Figure 7: i.e., the density oscillations are predominately inside the (original) loop structure. We conclude that this is because there is insufficient impulsive velocity in the *x-z* plane to significantly displace the loop (in the model presented here).

The work performed in this paper has highlighted the importance of including individual loop density structure in the modeling of active regions and has illustrated the need for obtaining accurate density measurements for coronal seismology. Future work will involve extending this technique to include more complicated loop structures, such as a nonuniform density across the loop, and the inclusion of multiple loops (recent work in this area includes Ofman 2005; Luna et al. 2006; Gruszecki et al. 2006; Selwa et al. 2006; Arregui et al. 2008). In addition, we will extend our curved coronal loop model to include a thin boundary layer, whereby its internal density blends into the external environment. This will allow us to fully investigate the additional damping due to resonant absorption, but will require a significant increase in numerical resolution in order to fully resolve the boundary layers.

Finally, the work here aims to contribute to one of the unanswered questions of coronal seismology: why are only a small number of loops seen to oscillate in *TRACE* observations? Our contribution here is twofold; first, the strong magnetic field in the active region reflects and refracts the impulsive wave away from the active region, and the resultant velocities inside the active region are several orders of magnitude less than the initial disturbance (as seen here and originally seen in Ofman & Thompson 2002); i.e., the loops inside the active region are in effect *shielded* from the impulsive fast wave by the high Alfvén speed region that they exist in. Secondly, we have shown here that the inclusion of a high-density loop in the surrounding magnetized plasma can support localized trapped MHD modes and that the damping time of these waves depends on the density contrast. We have found that loops with a higher density contrast have a longer damping time, but correspondingly have a much smaller amplitude. Thus, it is possible that some high-density loops in the corona are oscillating, but with amplitudes below that which can be seen with the resolution of *TRACE*.

Observations of wave activity in active regions combined with three-dimensional theoretical modeling can be used as a wave diagnostic for coronal parameters. It is hoped that the work performed here has contributed to such models. However, our observations are currently confined to line-of-sight imaging. The new *STEREO* spacecraft will provide stereoscopic information on the solar corona, and the resulting reconstruction will give us three-dimensional information on the loop structure. Also, high temporal and spatial resolution spectral images from the *Hinode* EIS instrument will provide additional insight. These new observations will allow new comparisons to be made between the data and theory and will further the development of our diagnostic tool for coronal active region parameters.

James McLaughlin wishes to thank Chris Brady, Alan Hood, Mag Selwa, and Jaume Terradas for helpful discussions. This work has been supported by the NASA SEC Theory program and NASA grant NNG06GI55G. Part of the computations reported in this work were performed on NASA Ames Columbia supercomputers.

APPENDIX A

STRAIGHT CYLINDER STUDY

In this appendix, we investigate the dependence of the amplitude and nature of oscillations in a straight cylinder on ξ. We consider a unidirectional magnetic field [$\boldsymbol{B} = B_0(0, 0, 1)$ in our nondimensionalized units, where B_0 is a constant] and define our loop as a cylinder of radius 0.5 and length 7.0, with density enhancement ξ; i.e., the density outside the cylinder is $\rho_0 = 0.1$ everywhere, and inside there is a discontinuous jump to $\rho_i = \xi/10$. This can be seen on the left-hand side of Figure 10. Equations (1)–(4) are solved in a computational box of dimensions $(x_{\min}, x_{\max}) \times (y_{\min}, y_{\max}) \times (z_{\min}, z_{\max})$, where $-x_{\min} = x_{\max} = -y_{\min} = y_{\max} = 1.5L$, $z_{\min} = 0$, and

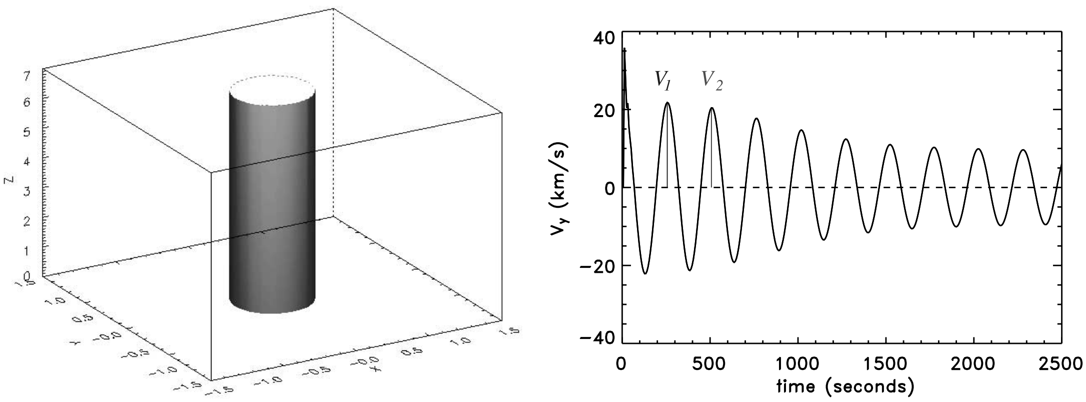

FIG. 10.—*Left*: Our cylindrical loop of length 7.0, radius 0.5, and density enhancement ξ relative to the (constant) background density, embedded in the unidirectional magnetic field B_z. *Right*: Time evolution of $V_y(0,\ 0,\ 3.5)$ in the $\xi = 2$ straight loop. The phase before (approximately) $t = 100$ s is the response to the incoming perturbation. The transient phase (or impulsive leaky phase) occurs until $t \approx 1500$ s, and the remaining part of the series represents the signature of the normal mode being established (stationary state). We use the amplitudes V_1 and V_2 to calculate a damping time. [*See the electronic edition of the Journal for a color version of this figure.*]

$z_{\max} = 7L$. The resolution used in the simulations shown here was $140 \times 140 \times 98$. We want to compare this straight loop with the numerical simulations of our curved loop, and so we choose $B_0 = 22$ G, where this choice sets $V_1(0,\ 0,\ 3)|_{\rm curved} = V_1(0,\ 0,\ 3.5)|_{\rm straight}$ for $\xi = 10$. This gives a typical speed of $V_0 = 1515.1$ km s^{-1} and an Alfvén time of $\tau_{\rm A} = 45.9$ s. We use the boundary conditions as described in § 2.1. We set $\beta = 0.01$ (Priest 1982) and ignore gravitational effects. We drive a wave pulse of the form given in equation (12) into our computational domain.

We find that the loop is impulsively excited by the fast wave. On the right-hand side of Figure 10, we see the temporal evolution of $V_y(0,\ 0,\ 3.5)$; i.e., the center of our box and midpoint of our loop. The temporal evolution consists of three stages. The first 100 s show the passage of the initial pulse. This is followed by a second stage (lasting until $t \approx 1500$ s), which is called the transient phase (or impulsive leaky phase), and thirdly, after $t \approx 1500$ s, we see the establishment of a single trapped mode (called the stationary state). The transient phase consists of the normal mode plus nontrapped modes, and these transient modes are damped due to wave leakage. The leakage rate in the transient phase is determined by the density contrast.

In the stationary state, the trapped mode has a much smaller damping rate due to (small) numerical dissipation, but this damping rate is approximately an order of magnitude less than the leakage rate in the transient phase. This numerical damping is constant throughout the simulation, but the damping rate changes between the transient phase and stationary state. Hence, numerical damping cannot explain the damping in both phases, but dividing the oscillation into a transient and stationary phase provides a natural explanation for the change in the damping rate.

Similar behavior was observed by Terradas et al. (2006b), in which several phases were found when studying how initial disturbances induce kink-mode oscillations in 1D and 2D line-tied cylindrical loops: two initial extrema followed by short-period oscillations that are quickly attenuated (transient phase), leading to the establishment of a long-period oscillation (stationary state). The transient stage was also seen in numerical work by Steinolfson & Davila (1993). However, our paper is the first work that models 3D MHD nonlinear loop oscillations with the excitation described in § 2.1, and so the work of Terradas et al. (2006b) cannot be directly compared to our mode excitation mechanism. Steinolfson & Davila (1993) also solves linear MHD equations, and in that work only normal modes are excited in a driven problem. Hence, the results of both papers are excellent guides for the nature of the transient phase, but cannot be directly applied to our model.

As in § 4, we consider the amplitudes V_1 and V_2 and calculate V_1/V_2, the period of oscillation, and the damping time as functions of ξ. The results can be seen in Figure 9. In Figure 9*a*, we see that the velocity amplitude decreases with increasing ξ. From Figure 9*b*, we see that the ratio of V_1 to V_2 is not constant and increases approximately linearly with ξ. In Figure 9*c*, we see that the period increases with increasing ξ, and that the agreement with the analytical work of Edwin & Roberts (1983) is very good. In Figure 9*d*, we see that the damping time decreases with increasing density contrast. This is in some agreement with equation (17), which is from the resonant absorption models of Ionson (1978), Hollweg & Yang (1988), and Ruderman & Roberts (2002), although, as mentioned above, the damping mechanism here is not due to resonant absorption, as we do not have thin layers at the cylinder boundary. These trends are the key results from this appendix. The results from this appendix are used in § 4.4, which compares this straight loop model with the curved loop model.

APPENDIX B

ANALYTICAL WORK

The WKB (Wentzel-Kramers-Brillouin) approximation was derived for the Schrödinger equation in 1926 for slowly varying amplitude and phase of the wave. Here we use this approach to discuss the reflection/transmission coefficient utilized in § 4.4. Under the WKB approximation, the energy flux of the Alfvén wave is $(1/2)\rho\,\delta v^2\, V_{\rm A} =$ constant. Substituting in normalized units, $V_{\rm A} = B/\rho^{1/2}$, and assuming that B is constant over the distance the wave travels gives

$$\rho^{1/2}\,\delta v^2 = \text{constant} \qquad \Rightarrow \qquad \delta v \sim \rho^{-1/4}.$$

The reflection/transmission coefficient at the loop boundary is calculated as follows. Consider a 1D wave impacting on a boundary (located at $x = 0$) such that it is partially reflected and partially transmitted. Let the waves be of the form $\sim e^{i(kx-\omega t)}$, and let R be the reflection coefficient and T be the transmission coefficient. Here ω is the frequency of the wave and k_0 and k_i are the wavevectors in the mediums on either side of the boundary, where the subscript "0" denotes "outside" and the subscript "i" denotes "inside." Let the region in which the wave starts and is reflected back into have density ρ_0 and the region into which the wave is transmitted have density ρ_i. Thus, continuity at the boundary dictates that

$$e^{i(k_0x-\omega t)} + Re^{i(-k_0x-\omega t)} = Te^{i(k_ix-\omega t)},$$
$$\text{such that at } x = 0, \qquad 1 + R = T. \tag{B1}$$

Matching derivatives at the boundary gives

$$ik_0e^{i(k_0x-\omega t)} - ik_0Re^{i(-k_0x-\omega t)} = ik_iTe^{i(k_ix-\omega t)},$$
$$\text{such that at } x = 0, \qquad 1 - R = T\frac{k_i}{k_0}. \tag{B2}$$

Now assume that $\omega/k_0 = v_0 = \alpha\rho_0^{-1/2}$, where α is a constant of proportionality, and assume a similar expression inside the boundary. This implies that $k_i/k_0 = (\rho_i/\rho_0)^{1/2}$. Hence, adding equations (B1) and (B2) gives

$$T = \frac{2}{1+\sqrt{\rho_i/\rho_0}} = \frac{2}{1+\sqrt{\xi}}, \qquad \text{where } \xi = \frac{\rho_i}{\rho_0}.$$

REFERENCES

Arregui, I., Andries, J., Van Doorsselaere, T., Goossens, M., & Poedts, S. 2007, A&A, 463, 333
Arregui, I., Terradas, J., Oliver, R., & Ballester, J. L. 2008, ApJ, 674, 1179
Arregui, I., Van Doorsselaere, T., Andries, J., Goossens, M., & Kimpe, D. 2005, A&A, 441, 361
Aschwanden, M. J. 2003, in Turbulence, Waves, and Instabilities in the Solar Plasma, ed. R. Erdélyi et al. (Dordrecht: Kluwer), 215
———. 2004, Physics of the Solar Corona: An Introduction (Berlin: Springer)
Aschwanden, M. J., De Pontieu, B., Schrijver, C. J., & Title, A. M. 2002, Sol. Phys., 206, 99
Aschwanden, M. J., Fletcher, L., Schrijver, C. J., & Alexander, D. 1999, ApJ, 520, 880
Aschwanden, M. J., Nightingale, R. W., Andries, J., Goossens, M., & Van Doorsselaere, T. 2003, ApJ, 598, 1375
Ballai, I. 2007, Sol. Phys., 246, 177
Banerjee, D., Erdélyi, R., Oliver, R., & O'Shea, E. 2007, Sol. Phys., 246, 3
Brady, C. S., & Arber, T. D. 2005, A&A, 438, 733
Brady, C. S., Verwichte, E., & Arber, T. D. 2006, A&A, 449, 389
Cirtain, J., Martens, P. C. H., Acton, L. W., & Weber, M. 2006, Sol. Phys., 235, 295
Davila, J. M. 1987, ApJ, 317, 514
De Moortel, I. 2005, Philos. Trans. R. Soc. London A, 363, 2743
Díaz, A. J. 2006, A&A, 456, 737
Díaz, A. J., Zaqarashvili, T., & Roberts, B. 2006, A&A, 455, 709
Edwin, P. M., & Roberts, B. 1983, Sol. Phys., 88, 179
Erdélyi, R., & Verth, G. 2007, A&A, 462, 743
Gary, G. A. 2001, Sol. Phys., 203, 71
Goossens, M., Andries, J., & Aschwanden, M. J. 2002, A&A, 394, L39
Goossens, M., Hollweg, J. V., & Sakurai, T. 1992, Sol. Phys., 138, 233
Goossens, M., Ruderman, M. S., & Hollweg, J. V. 1995, Sol. Phys., 157, 75
Gruszecki, M., Murawski, K., Selwa, M., & Ofman, L. 2006, A&A, 460, 887
Gruszecki, M., Murawski, K., Solanki, S. K., & Ofman, L. 2007, A&A, 469, 1117
Heyvaerts, J., & Priest, E. R. 1983, A&A, 117, 220
Hollweg, J. V. 1987, ApJ, 312, 880
Hollweg, J. V., & Yang, G. 1988, J. Geophys. Res., 93, 5423
Ionson, J. A. 1978, ApJ, 226, 650
Luna, M., Terradas, J., Oliver, R., & Ballester, J. L. 2006, A&A, 457, 1071
McLaughlin, J. A., & Hood, A. W. 2004, A&A, 420, 1129
———. 2006, A&A, 452, 603
McLaughlin, J. A., & Ofman, L. 2006, in Proc. *SOHO*-17: 10 Years of *SOHO* and Beyond, ed. H. Lacoste (ESA SP-617; Noordwijk: ESA), 103
Murawski, K., Selwa, M., & Nocera, L. 2005, A&A, 437, 687
Nakariakov, V. M., & Ofman, L. 2001, A&A, 372, L53
Nakariakov, V. M., Ofman, L., DeLuca, E., Roberts, B., & Davila, J. M. 1999, Science, 285, 862
Nakariakov, V. M., & Roberts, B. 1995, Sol. Phys., 159, 399
Nakariakov, V. M., & Verwichte, E. 2005, Living Rev. Sol. Phys., 2, 3, http://www.livingreviews.org/lrsp-2005-3
Nakariakov, V. M., Verwichte, E., Berghmans, D., & Robbrecht, E. 2000, A&A, 362, 1151
Ofman, L. 2005, Adv. Space Res., 36, 1572
———. 2007, ApJ, 655, 1134
Ofman, L., & Aschwanden, M. J. 2002, ApJ, 576, L153
Ofman, L., & Davila, J. M. 1995, J. Geophys. Res., 100, 23427
Ofman, L., Davila, J. M., & Steinolfson, R. S. 1994, ApJ, 421, 360
———. 1995, ApJ, 444, 471
Ofman, L., & Thompson, B. J. 2002, ApJ, 574, 440 (Paper I)
Ofman, L., & Wang, T. J. 2008, A&A, 482, L9
Poedts, S., & Kerner, W. 1991, Phys. Rev. Lett., 66, 2871
Priest, E. R. 1982, Solar Magneto-hydrodynamics (Dordrecht: Reidel)
Roberts, B. 1981, Sol. Phys., 69, 27
———. 2000, Sol. Phys., 193, 139
———. 2004, in Proc. *SOHO*-13: Waves, Oscillations and Small-Scale Transient Events in the Solar Atmosphere: A Joint View of *SOHO* and *TRACE*, ed. H. Lacoste (ESA SP-547; Noordwijk: ESA), 1
Roberts, B., Edwin, P. M., & Benz, A. O. 1983, Nature, 305, 688
———. 1984, ApJ, 279, 857
Ruderman, M. S., & Roberts, B. 2002, ApJ, 577, 475
Selwa, M., Murawski, K., & Solanki, S. K. 2005a, A&A, 436, 701
Selwa, M., Murawski, K., Solanki, S. K., & Wang, T. J. 2007, A&A, 462, 1127
Selwa, M., Murawski, K., Solanki, S. K., Wang, T. J., & Tóth, G. 2005b, A&A, 440, 385
Selwa, M., Solanki, S. K., Murawski, K., Wang, T. J., & Shumlak, U. 2006, A&A, 454, 653
Smith, J. M., Roberts, B., & Oliver, R. 1997, A&A, 317, 752
Steinolfson, R. S., & Davila, J. M. 1993, ApJ, 415, 354
Taroyan, Y., Erdélyi, R., Wang, T. J., & Bradshaw, S. J. 2007, ApJ, 659, L173
Terradas, J., & Ofman, L. 2004, in Proc. *SOHO*-13: Waves, Oscillations and Small-Scale Transient Events in the Solar Atmosphere: A Joint View of *SOHO* and *TRACE*, ed. H. Lacoste (ESA SP-547; Noordwijk: ESA), 469
Terradas, J., Oliver, R., & Ballester, J. L. 2005a, ApJ, 618, L149
———. 2005b, A&A, 441, 371
———. 2006a, Philos. Trans. R. Soc. London A, 364, 547
———. 2006b, ApJ, 650, L91
Tomczyk, S., McIntosh, S. W., Keil, S. L., Judge, P. G., Schad, T., Seeley, D. H., & Edmondson, J. 2007, Science, 317, 1192
Uchida, Y. 1970, PASJ, 22, 341
Van Doorsselaere, T., Debosscher, A., Andries, J., & Poedts, S. 2004, A&A, 424, 1065
Van Doorsselaere, T., Nakariakov, V. M., & Verwichte, E. 2007, A&A, 473, 959
Verth, G., Van Doorsselaere, T., Erdélyi, R., & Goossens, M. 2007, A&A, 475, 341
Verwichte, E., Foullon, C., & Nakariakov, V. M. 2006a, A&A, 446, 1139
———. 2006b, A&A, 449, 769
Wang, T. J., Innes, D. E., & Qiu, J. 2007, ApJ, 656, 598
Wang, T. J., & Solanki, S. K. 2004, A&A, 421, L33
Wang, T. J., Solanki, S. K., Curdt, W., Innes, D. E., Dammasch, I. E., & Kliem, B. 2003a, A&A, 406, 1105
Wang, T. J., Solanki, S. K., Innes, D. E., Curdt, W., & Marsch, E. 2003b, A&A, 402, L17
Williams, D. R., Mathioudakis, M., Gallagher, P. T., Phillips, K. J. H., McAteer, R. T. J., Keenan, F. P., Rudawy, P., & Katsiyannis, A. C. 2002, MNRAS, 336, 747
Williams, D. R., et al. 2001, MNRAS, 326, 428